

Design of Longitudinal Control for Reduced-Gravity Atmospheric Flights

Yi-Hsuan Chen* and Eric Feron†

King Abdullah University of Science and Technology, Thuwal, Saudi Arabia

Reduced-gravity environments created by airplanes have a wide range of potential applications, such as astronaut training and scientific research in zero- or partial- gravity levels. Reduced-gravity flights, casually called parabolic flights, can be achieved by making aircraft follow specific trajectories. This work describes the physics behind reduced-gravity flights and develops a flight control framework for a zero-gravity flight using a proof-mass-tracking approach. During the zero-gravity parabola phase, aircraft has a zero local (non-gravitational) acceleration and be in a state of free-fall, thus causing the sensation of weightlessness. Hence, the control objective is to simultaneously compensate for aerodynamic drag using thrust control and to make lift force zero by regulating the aircraft with the elevator. A triple-integral control structure is adopted to overcome the unknown drag that is expected to grow quadratically with time. Moreover, the position deviation from the reference object is measured in the cockpit to enable a better control performance. Flight simulations are performed and visualized to illustrate the proposed control strategy.

I. Nomenclature

CG	= center of gravity
AR	= aspect ratio
\mathcal{F}_E	= Earth-fixed inertial frame (x^E, y^E, z^E)
\mathcal{F}_B	= body-fixed frame (x^B, y^B, z^B)
\mathcal{F}_S	= stability frame (x^S, y^S, z^S)
g	= gravitational acceleration constant on Earth
Q	= dynamic pressure
α	= angle of attack (AOA)
γ	= flight path angle
θ	= pitch angle
u	= velocity component of the CG along the x^B axis
w	= velocity component of the CG along the z^B axis
q	= pitch rate of the CG along the y^B axis
ω	= angular velocity vector of the CG in frame \mathcal{F}_B
x	= position component of the CG along the x^E axis
z	= position component of the CG along the z^E axis
h	= altitude of the CG directed along the $-z^E$ axis
L	= lift force
D	= drag force
W	= weight
T	= thrust
δ_e	= elevator deflection
$M(\delta_e)$	= pitch moment
X	= non-gravitational force acting along the x^B axis
Z	= non-gravitational force acting along the z^B axis
a_x	= “local” (non-gravitational) acceleration component of the CG along the x^B axis

*Graduate Research Assistant, Mechanical Engineering, yihsuan.chen@kaust.edu.sa

†Professor, Electrical, Computer, and Mechanical Engineering, eric.feron@kaust.edu.sa, AIAA fellow

a_z	=	"local" (non-gravitational) acceleration component of the CG along the z^B axis
n_x	=	load factor along the x^B axis
n_z	=	load factor along the z^B axis
$g\text{-level}$	=	an index for evaluating the magnitude of local acceleration
V_o	=	nominal velocity
γ_o	=	nominal flight path angle
e_t	=	local tangential position error along the x^B axis in frame \mathcal{F}_B
e_n	=	local normal position error along the $-z^B$ axis in frame \mathcal{F}_B
λ	=	terrestrial longitude
ϕ	=	geodetic latitude
V_N	=	geographic system north component of velocity over Earth
V_E	=	geographic system east component of velocity over Earth

II. Introduction

REDUCED-gravity flights not only serve as a means for astronaut training but also contribute to a wide variety of research fields such as fundamental physics, material science, and biomedical technology [1], paving the way for taking humans farther into the solar system. Various platforms can be used to create microgravity, and each platform generates different levels and durations, ranging from a few seconds to several months. Considering the reduced-gravity flights, the reduced-gravity phase is generally achieved 30-60 times in an approximately 3-hour flight [2] as the aircraft follows a trajectory where low gravity is "felt" in the reference frame of the vehicle. Zero-g flight is the most popular form of reduced- g flights, and it can be achieved when the aircraft follows exactly a part of a low Earth orbit [3]. Currently, there are two companies offering gravity-free flights, that is, the Airbus A310 Zero G in France operated by Novespace [4] and the modified Boeing 727 G-FORCE ONE operated by Zero-G [5]. Note that the actual flown trajectories are not exactly parabolic but are elliptical; however, the flight maneuvers performed to simulate reduced gravity are still called parabolic [6] to acknowledge Earth's gravity is locally constant.

Even though reduced-gravity flights have already demonstrated their potential as Earth-based microgravity research platforms, there is still room for improvement in the quality and duration of the reduced gravity experiments [7]. As parabolic maneuvers are generally operated manually, the quality and period of reduced gravity depend significantly on the pilots' skills and weather conditions. Hence, this paper aims to explore the possibility of creating microgravity with the help of the automatic flight control system, which not only allows us to provide consistent reduced-gravity conditions but also opens up new possibilities of microgravity enabling fixed-wing unmanned aerial vehicles.

Our proposed control logic is inspired by a proof-mass-tracking scenario commonly used in drag-free satellites [8, 9]. This paper concentrates on fixed-wing vehicle and builds upon Afman's works in developing flight control algorithms for a quadrotor [10–12]. The position of an aircraft with respect to the proof mass is constantly measured in frame \mathcal{F}_B and fed back to the proposed controller, whose action results in the aircraft following the purely gravitational orbit provided by the proof mass.

The advantage of using a free-floating proof mass is that it only requires the position deviation between the aircraft and the proof mass to guide the vehicle to follow a drag-free trajectory, thus reducing the dependence on measurements of aircraft states [13, 14]. One of the key features of the proposed control strategy is that we use triple-integral control combined with state feedback to regulate the aircraft to the nominal drag-free trajectory.

III. Reduced-Gravity Flight Background

There are several ways to simulate reduced gravity on Earth, such as drop towers, parabolic flights, and ground-based experimental devices [15]; for instance, Sanavandi and Guo developed a novel magnetic levitation-based low-gravity simulator to serve as a durable and low-cost microgravity research platform [16]. Drop towers and reduced- g flights are two most popular Earth-based ways to simulate near-space conditions. The critical drawbacks with drop towers are the short test duration, generally 2-9 seconds [10], which is limited by the height of towers, and the considerable upfront cost of necessary infrastructure. In contrast, reduced- g flights provide low-gravity conditions with durations ranging from 20 to 40 seconds. Furthermore, although reduced- g flights require higher operating costs, the capital expenditures on infrastructure are lower compared to drop towers. Also, they hold several competitive advantages over drop towers, including the longer duration of reduced gravity, the capability of providing partial gravity and accommodating large-scale experiments, and the accessibility to hypergravity before and after reduced-gravity period.

A. Related research work in reduced-gravity aerial vehicles

Several studies on the design of control systems for reduced-gravity flight exist in the literature. For instance, Mora-Camino and Achaibou [17] proposed a nonlinear inverse control law combined with a sliding controller under the assumption of a constant throttle setting to improve the accuracy and duration of zero-gravity flights. Amato et al. [18] performed a control scheme based on an online evaluation of the aircraft command signals needed to regulate longitudinal and vertical load factors to zero, but the method has been reported to be computationally cumbersome. Thus, an alternative to solve the nonlinear dynamic optimization problem was demonstrated in their follow-up work [19]. Furthermore, the authors developed a control action consisting of a feedforward part guaranteeing good tracking performance in the absence of external disturbances and feedback term employing gain-scheduled output feedback to counteract possible misalignments. D'Antonio and Monaco [20] designed a nonlinear controller based on dynamical feedback linearization to track a given parabolic trajectory.

Comprehensive theoretical analysis for the dynamics of parabolic flight involving flight characteristics and passengers' perceptions can be found in [2], which inspired Hathaway and Jacob [14] to explore multiple options for microgravity controllers. One approach is to equalize the throttle to the estimated drag and regulate the flight path angle to the nominal angle along the ballistic trajectory. Another approach is to modulate lift force using elevator deflection. However, the main challenge of these approaches is that drag is speed-dependent and cannot be easily measured nor estimated.

Other works on developing assisted flights simulators to help the pilot execute the maneuver precisely can be found in [21] and [22]. Hosman and Kunen [21] presented flight director control laws incorporating a gain scheduler, a predictor, and a sequencer to optimize the quality and duration of reduced-gravity conditions and to guarantee that the limitations of aircraft were not exceeded. Brigos et al. [22] designed a computer simulator built on experimental data from test flights to reproduce parabolic maneuvers to train aerobatic pilots.

Recently, Unmanned Aerial Vehicles (UAVs) have shown potential to be extended as a microgravity research platform due to their increased availability and reliability. Early conceptual studies on fixed-wing UAVs can be found in [13] and [23]. A Proportional-Integral (PI) pitch rate controller was proposed to continuously track the changing pitch rate along the desired partial gravity trajectory, and an autonomously flown torque-controlled free-wing UAV was subsequently designed to enable accurate microgravity maneuvers and decrease gust sensitivity. Experimental flight tests were reported in [24] and [25], thus demonstrating the viability of using small UAVs as microgravity enabling platforms.

Unlike fixed-wing aircraft, multi-rotors have the advantage of being able to perform simple 1-D vertical reduced-gravity maneuvers. Afman et al. [10–12] devised a Proportional–Integral–Ramp–Quadratic (PIRQ) control architecture to reject quadratic drag disturbances, which was experimentally validated through flight tests on a variable-pitch quadrotor by performing a Martian parabola. The maneuver regulation approach and theoretical stability analysis using transverse dynamics coordinate are detailed in [11, 26]. Kedarisetty established various approaches using a multirotor to realize a constant gravity level, such as a gain compensation which varies the autopilot gains to counter the negative effect of rotor aerodynamics [27], a nonlinear controller combined feedback linearization with sliding mode control to improve robustness [28], and a differential flatness-based acceleration control law augmented with a parameter estimation scheme to achieve high accuracy [29].

However, the downside of multirotors is the short duration of the microgravity phase of flight. Thus, we are interested in designing a flight control framework for fixed-wing aircraft that uses as little information as possible to handle reduced-gravity flights. This work adopts the proof-mass-tracking technique commonly used in drag-free satellites and extends the triple-integral control architecture presented in [12] to 2-D parabolic maneuvers for zero-g flights.

B. Reduced-gravity flight maneuver

Unlike commercial flights, reduced-gravity flights require specially trained pilots and instrumentation to achieve a high level of reduced-gravity precision. The maneuver is executed by three pilots simultaneously. The first pilot controls the pitch angle to maintain the required g -level. The second pilot counters any movement in the roll axis and keeps the wings level. The third pilot sits between the other two and adjusts the thrust levers to maintain the required level of thrust during the maneuver [30, 31]; refer to Fig. 1.

Depending on the level of low gravity desired, the reduced-gravity environment can be maintained during the maneuver for between 20 and 40 seconds within an aircraft flown along a precise trajectory that resembles an inverted parabola. The typical zero- g maneuver is divided into the four stages of preparation, pull-up, parabola (or pushover), and recovery, with each phase at a different g -level, see Fig. 2.



Fig. 1 The Airbus ZERO-G performing a microgravity parabola (Credits: European Space Agency)

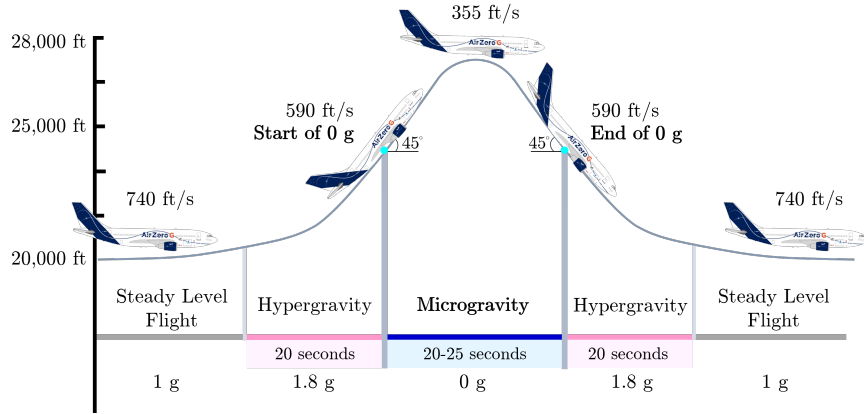


Fig. 2 Zero-gravity flight maneuver stage breakdown (Adapted from [31])

The aircraft begins the preparation phase in 1 g level flight and accelerates to specific airspeed and altitude entry parameters. Once these parameters are achieved, the pull-up is initiated by smooth application of the aft movement of the control yoke to attain between 1.5-1.8 g. This pull-up phase leads to the maximum pitch attitude of the maneuver at the planned entry altitude and airspeed, which triggers initiation of the reduced-gravity parabolic portion of the maneuver. One pilot smoothly pushes forward on the yoke to attain and maintain the required g-level, reducing the angle of attack, which results in a decrease in lift. Simultaneously, another pilot reduces thrust to a level just sufficient to overcome drag. It should be noted that in reduced-g flights, stall speed is equal to unaccelerated stall speed scaled by the square root of the load factor (or g) divided by the total aircraft weight. This implies that stall does not occur in zero-g since the wings are not generating any lift. Also, notice that the microgravity phase of flight starts while the aircraft is climbing and does not only happen when descending. During the initial microgravity phase, the aircraft has upward velocity, but downward acceleration whose magnitude is equal to standard gravity [2].

After a 20-40 second reduced-gravity trajectory has elapsed, the negative pitch rate required to maintain the reduced-gravity environment leads to the maneuver's maximum pitch-down attitude $\theta = -45^\circ$ and the recovery phase begins. One pilot recovers the aircraft from the dive by smoothly reversing forward deflection of the yoke to aft deflection to attain approximately 1.8-2 g, while another pilot adjusts the thrust to avoid airframe overspeed and returns to 1 g level flight. In order to reduce pilot workload in operating this specific maneuvers and improve the quality and duration of the reduced-gravity phase, we study the dynamics of parabolic flights and then propose a automatic flight control system.

C. Inspiration from drag-free satellite

To develop our flight control framework, we choose to implement the concept of proof-mass-tracking to generate the desired zero-g trajectory from any initial condition. The proof mass is an object inside a completely enclosed chamber

within a vehicle, protected from the atmosphere by the vehicle itself, and is only subject to gravity. The drag-free satellite tracks and maintains its position relative to the proof mass falling in its interior in order to maintain a perfect weightless environment. Similarly, a pilot is able to hold a proof mass in their hand at the beginning of a pushover, float the proof mass above their hand, and then maintain the proof mass in exactly the same position relative to the aircraft during the maneuver. This allows the pilot to use the flight controls to maintain a zero-g environment inside the aircraft, as long as the aircraft is kept in the same position relative to the proof mass. This scenario is supported in the absence of any air conditioning or other cockpit environment-induced forces on the proof mass. Therefore, an autopilot with a way to track and maintain its position relative to a proof mass would be able to use the same principles to generate a zero-g environment. The position errors appear when we deviate from the nominal trajectory and can be used as the controller input to calculate the required thrust and elevator deflection to eliminate the deviation between the cockpit and the proof mass, as shown in Fig. 3.

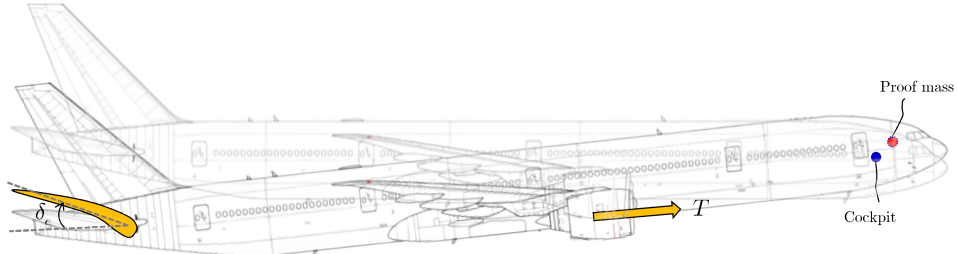


Fig. 3 Proof-mass-tracking scenario by regulating thrust and the elevator

IV. Dynamic Analysis of Reduced-Gravity Flight

This section studies the longitudinal equations of motion to analyze the perception of acceleration that objects inside the aircraft experience during flight. Two longitudinal models are presented for different purposes. More specifically, in this work, the stability-axes model is used to design an automatic flight control system, while the body-axes model is used to study the relationship between external forces and local acceleration.

A. Longitudinal equations of motion

We assume that the body x^Bz^B plane is a plane of symmetry, which means lateral velocity v , roll rate p , and yaw rate r are negligible; roll and sideslip angles, ϕ and β , are zero during the parabolic maneuver. Thus, a 6-DoF model could be decoupled to a 3-DoF model describing pure longitudinal motion. First, for the purpose of studying the dynamic behavior along the nominal reduced-gravity trajectory, velocity equations in terms of the stability-axes variables, airspeed and aerodynamic angles, are adopted. On the other hand, for analyzing the connection between the forces acting on an airplane and the sensation of weight, the state equation expressed in terms of velocity components in the aircraft body frame is the better choice [32]. A typical control vector of the longitudinal model is $\mathbf{U} = (T, \delta_e) \in \mathbb{R}^2$, where T is engine thrust and δ_e is elevator deflection. We present two 3-DoF longitudinal models in the following page. For the more detailed mathematical derivation of aircraft longitudinal dynamics, we refer the reader to [32] and [33]. Figure 4 illustrates the definition of aerodynamic forces, moment, and angles.

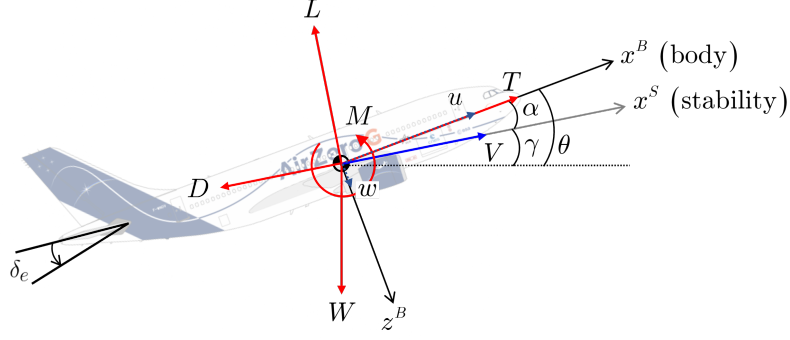


Fig. 4 Longitudinal forces, moments, and angles

We introduce two models:

- 1) Stability-axes longitudinal model with the state vector $\mathbf{X} = (V, \gamma, \theta, q) \in \mathbb{R}^4$

$$\dot{V} = \frac{1}{m} (-D + T \cos \alpha - mg \sin \gamma) \quad (1)$$

$$\dot{\gamma} = \frac{1}{mV} (L + T \sin \alpha - mg \cos \gamma) \quad (2)$$

$$\dot{\theta} = q \quad (3)$$

$$\dot{q} = \frac{M(\delta_e)}{I_y} \quad (4)$$

- 2) Body-axes longitudinal model with the state vector $\mathbf{X} = (u, w, \theta, q) \in \mathbb{R}^4$

$$\dot{u} = \frac{X}{m} - g \sin \theta - qw \quad (5)$$

$$\dot{w} = \frac{Z}{m} + g \cos \theta + qu \quad (6)$$

$$\dot{\theta} = q \quad (7)$$

$$\dot{q} = \frac{M(\delta_e)}{I_y} \quad (8)$$

where m and I_y are the mass and the moment of inertia about pitch axis, V is the aerodynamic velocity, γ is the flight path angle, θ is the pitch angle, q is the pitch rate, u and w are the velocity components in frame \mathcal{F}_B , T is engine thrust, δ_e is elevator deflection, and L , D , and M denote the aerodynamic lift, drag, and pitch moment, respectively. The definition of angle of attack is $\alpha = \theta - \gamma$. X and Z represent non-gravitational forces acting along the body axes x^B and z^B [33], which can be written as

$$X = T + L \sin \alpha - D \cos \alpha \quad (9)$$

$$Z = -L \cos \alpha - D \sin \alpha \quad (10)$$

The aerodynamic forces and moment are defined in terms of dimensionless lift, drag, and pitch moment coefficients C_L , C_D , C_m , the dynamic pressure Q , reference wing area S , and the characteristic length \bar{c} as

$$L = QSC_L, \quad D = QSC_D, \quad M = QS\bar{c}C_m \quad (11)$$

where $Q = \frac{1}{2}\rho V^2$ and ρ is the air density. The dimensionless aerodynamic coefficients can be modeled as [34–36]

$$\begin{aligned} C_L &= C_{L_0} + C_{L_\alpha} \alpha + C_{L_q} \frac{q\bar{c}}{2V} + C_{L_{\delta_e}} \delta_e \\ C_D &= C_{D_0} + C_{D_\alpha} \alpha \\ C_m &= C_{m_0} + C_{m_\alpha} \alpha + C_{m_q} \frac{q\bar{c}}{2V} + C_{m_{\delta_e}} \delta_e \end{aligned} \quad (12)$$

where $C_{L_0}, C_{L_\alpha}, C_{L_q}, C_{L_{\delta_e}}, C_{L_0}, C_{m_0}, C_{m_\alpha}, C_{m_q}, C_{m_{\delta_e}}$ are longitudinal derivatives, and C_{D_i} denotes an induced-drag coefficient given by

$$C_{D_i} = \frac{C_L^2}{\pi A Re}$$

where AR is the aspect ratio and e is an efficiency factor, ranging between 0.7 and 0.85 typically.

B. Relationship between forces and local acceleration

Here we assume the body axes x^B and y^B define the floor plane of the aircraft and that the aircraft thrust is aligned with the $+x^B$ direction. In longitudinal motion, the “local” acceleration components expressed in the body-fixed coordinate can be derived based on the Newton–Euler Equations as [24].

$$a_x = \frac{X}{m} = \dot{u} + qw + g \sin \theta, \quad (13)$$

$$a_z = \frac{Z}{m} = \dot{w} - qu - g \cos \theta. \quad (14)$$

Note that the “local” acceleration is used to describe how much gravity we “feel” during flight, which can also be interpreted as the acceleration caused by non-gravitational forces. Then we can evaluate the load factors and then define the g -level as

$$n_x = \frac{a_x}{g}, \quad n_z = \frac{a_z}{g}, \quad g\text{-level } (g) = \sqrt{n_x^2 + n_z^2}. \quad (15)$$

Reduced gravity is the condition in which the gravity force felt locally within the aircraft is lower than normal gravity (1 g). In our case, the direction of the force is assumed to be orthogonal to the floor of the aircraft rather than to the flight path angle. That is, we desire zero tangential acceleration, $a_x = 0$, and some desired normal acceleration $a_z = -\mu g$ ($0 < \mu < 1$), implying that $X = 0$, $Z = -\mu mg$. Moreover, under the small angle-of-attack assumption, (9) and (10) can be simplified to

$$\begin{aligned} X &\approx T - D = 0 \\ Z &\approx -L = -\mu mg \end{aligned} \quad (16)$$

Therefore, we can conclude that, during the reduced-gravity flight, thrust should be controlled to compensate for drag. At the same time, lift needs to be regulated by adjusting the elevator to provide a certain level of gravity.

C. Non-minimum phase characteristics of the CG response to elevator inputs

The response of altitude change at the CG due to an elevator input has a non-minimum phase characteristic, which results from the process of generating a pitch-up moment that produces a small downward force, causing the center of gravity of an aircraft to lose altitude before going upwards [37]. The presence of non-minimum phase dynamics will degrade the performance of controllers. Related works on the control of non-minimum phase (NMP) aircraft systems may also be found in [38, 39]. One way to make longitudinal dynamics from elevator to the altitude of the proof mass minimum phase is to place the proof mass in the cockpit rather than the center of gravity of an aircraft. The similar technique was employed by Kim and Horspool [40] to convert the NMP longitudinal dynamics into a minimum phase system.

D. Kinematics of the cockpit

The kinematics of the CG of an aircraft during zero-g flight is known to satisfy projectile motion [13, 14], which can be expressed as

$$\begin{aligned} \ddot{x}(t) &= 0, \quad \dot{x}(t) = V_0, \quad x(t) = V_0 t \\ \ddot{z}(t) &= g, \quad \dot{z}(t) = gt, \quad z(t) = \frac{1}{2}gt^2 + z_0 \end{aligned} \quad (17)$$

where $(x, 0, z)$ is the position of the CG of aircraft in frame \mathcal{F}_E . Now we would like to extend the discussion to the motion of a rigid body in a two-dimensional plane to derive the position, velocity, and acceleration of the cockpit. $(\cdot)_c$ and $(\cdot)_p$ indicate the quantities at the CG and the cockpit, respectively.

Now consider an aircraft that is rotating with angular velocity ω about its CG, and the aircraft is simultaneously moving relative to the inertial frame (x^E, y^E, z^E) , refer to Fig. 5. Then, the equations of motion of the cockpit (point p) can be written in terms of the general expressions for relative motion (18), (19) and (20).

$$\mathbf{r}_p = \mathbf{r}_{cg} + \mathbf{r}_{p/cg} \quad (18)$$

$$\mathbf{v}_p = \mathbf{v}_{cg} + \mathbf{v}_{p/cg} = \mathbf{v}_{cg} + \boldsymbol{\omega} \times \mathbf{r}_{p/cg} \quad (19)$$

$$\mathbf{a}_p = \mathbf{a}_{cg} + \mathbf{a}_{p/cg} = \mathbf{a}_{cg} + \dot{\boldsymbol{\omega}} \times \mathbf{r}_{p/cg} + \boldsymbol{\omega} \times (\boldsymbol{\omega} \times \mathbf{r}_{p/cg}) \quad (20)$$

where $\mathbf{r}_p = (x_p, 0, z_p)$, \mathbf{v}_p , and \mathbf{a}_p are the position, velocity, and acceleration vectors of the cockpit with respect to the inertial frame; $\mathbf{r}_{cg} = (x, 0, z)$ is the position vector of the CG in frame \mathcal{F}_E ; and $\mathbf{r}_{p/cg}$, $\mathbf{v}_{p/cg}$, and $\mathbf{a}_{p/cg}$ are the position, velocity, and acceleration vectors of the cockpit as observed by the CG in frame \mathcal{F}_B . We also assume that the both the CG and the cockpit lie on the body x -axis x^B , meaning that $\mathbf{r}_{p/cg} = (d_x, 0, 0)$, for simplicity.

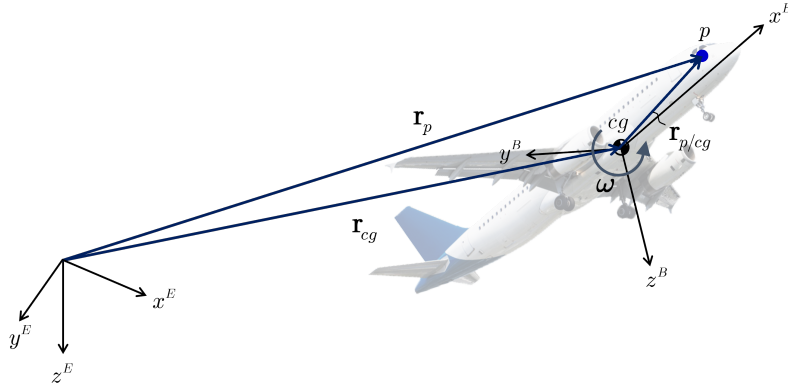


Fig. 5 The fixed point p (cockpit) in body frame is expressed in inertial frame

Here we illustrate the non-minimum phase characteristic by examining the altitude change at the CG and the cockpit of the aircraft due to the negative elevator impulse during level flight. The model used here is a Boeing 747 in steady-state level trimmed flight at $M = 0.25$ under sea-level conditions. As shown in Fig. 6a, the undershoot response of the CG altitude change due to the elevator impulse is the characteristic of an NMP system, thus causing some delays compared to a minimum-phase system (the cockpit's altitude change). We can also observe in Fig. 6b that when the elevator deflects up, the CG of an aircraft goes down initially due to the reduced lift in the CG before it climbs up. Thus, it is better to use position error measured at the cockpit as the feedback signal to enable a minimum phase system with elevator deflection input.

V. Development of a Control Framework for Zero-G Flight

We assume that the proof mass is placed inside a completely enclosed cavity in the cockpit; the position error between the proof mass and the aircraft (e_t, e_n) can be measured directly by an appropriate sensing apparatus. Note that the position error (e_t, e_n) is measured in the body-fixed frame \mathcal{F}_B . In order to keep the position of the cockpit fixed relative to free-falling proof mass, the position deviation is fed back to the controller, thus guiding the aircraft to follow the proof mass. More specifically, we design the thrust control loop to simultaneously produce a force equal and opposite to the drag to minimize the tangential error e_t and regulate the elevator to generate the moment to eliminate the normal error e_n . The closed-loop block diagram of our control framework is illustrated in Fig. 7, where $C_T(s)$ and $C_M(s)$ are the thrust and moment controllers, respectively.

A significant advantage of this method is that the aircraft does not follow a prescribed trajectory and tries to regulate itself around the nominal trajectory instead. In other words, after deviating from the nominal trajectory, the perturbed aircraft state is seen as a new initial condition for the next nominal trajectory. The reduced- g trajectory may be treated as an infinite number of initial conditions, together merging the entire trajectory. The similar regulation technique may also be found in [13].

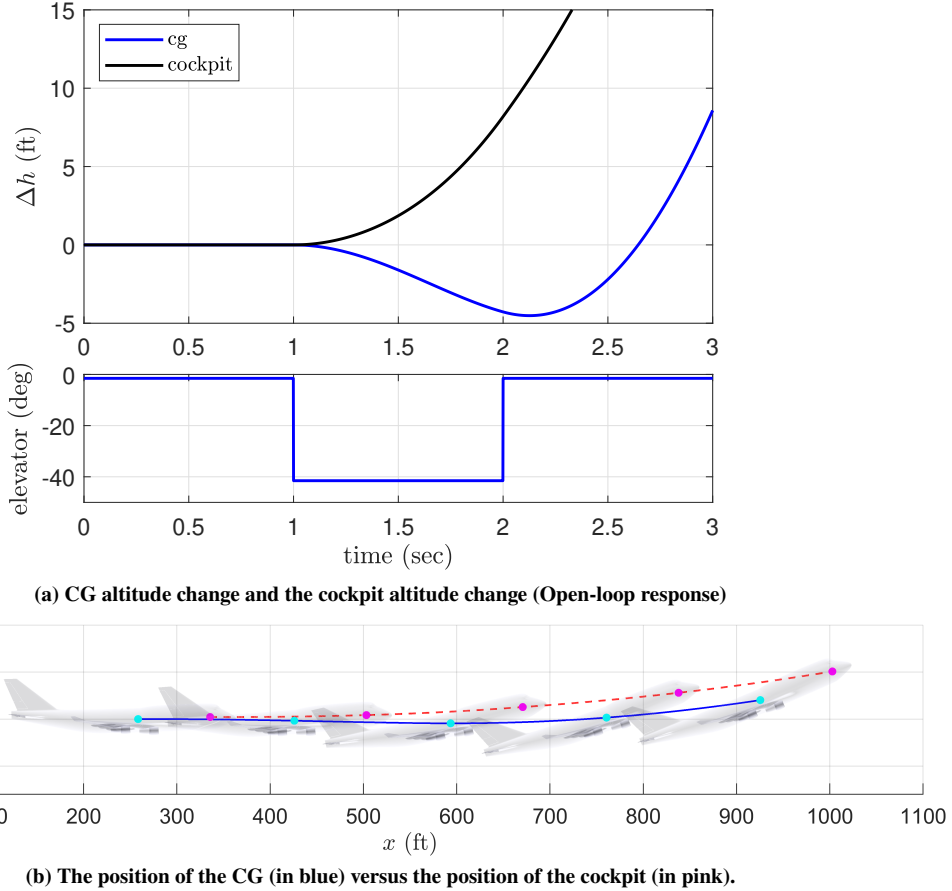


Fig. 6 Non-minimum phase behavior in pitch dynamics due to the elevator impulse (video link: <https://youtu.be/-SgGtaAJZ38>)

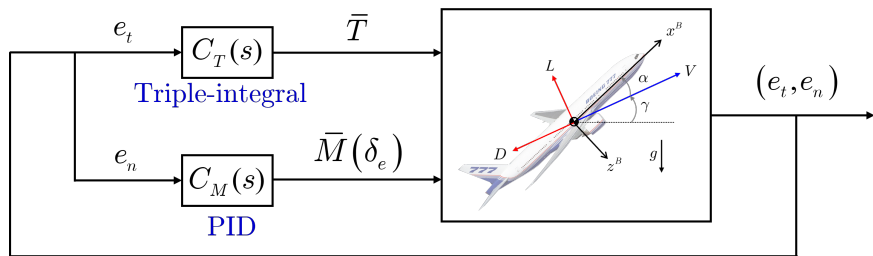


Fig. 7 Proposed control architecture for zero-gravity flight

A. Triple-integral thrust control

According to (16), we know that tracking a zero-g parabolic trajectory requires thrust force to counterbalance aerodynamic drag $D = QSC_D$. The term QSC_D , however, is speed-dependent and cannot be easily measured nor estimated. Thus, we aim to develop a thrust controller that has the ability to reject the unknown drag based on the characteristics of aerodynamic forces that evolve during parabolic flight. Recall the flight path of zero-g flight is exactly the trajectory of a projectile (17). Based on the definition of velocity, the true airspeed can be calculated as $V = \sqrt{\dot{x}^2(t) + \dot{z}^2(t)} = \sqrt{V_0^2 + g^2 t^2}$. Also, the dynamic pressure is $Q = \frac{1}{2}\rho V^2 = \frac{1}{2}\rho (V_0^2 + g^2 t^2)$. We find that the square of speed is a quadratic function of time, which causes dynamic pressure and drag to grow quadratically with time. Thus,

a triple-integral structure is adopted to counteract this unknown disturbance that is evolving quadratically with time. Moreover, we can validate the steady-state error of the controller composed of three integrators subject to a parabolic disturbance input by employing the Final Value Theorem

$$e(\infty) = \lim_{t \rightarrow \infty} e(t) = \lim_{s \rightarrow 0} sE(s)$$

The further details regarding tracking/rejecting higher-order signals/disturbances using integrators can be found in [12] and [41]. After realizing the necessity of the triple-integral control system, the next step is to implement this architecture in the aircraft velocity dynamics (21):

$$\dot{V} = \frac{1}{m} (T \cos \alpha - D - mg \sin \gamma) := \bar{T} - \hat{D} - g \sin \gamma \quad (21)$$

We make the following assumptions when designing the thrust controller:

- i) The angle of attack is small, i.e., $\alpha \approx 0$.
- ii) The derivative of the tangential position deviation can be approximated as the difference between actual and nominal velocity, i.e., $\dot{e}_t = V - V_o$.
- iii) Drag and gravitational forces are viewed as unknown disturbances, see Fig. 8.

As a result, the velocity dynamics considered in the controller design is $\dot{V} = \frac{T}{m} = \bar{T}$.

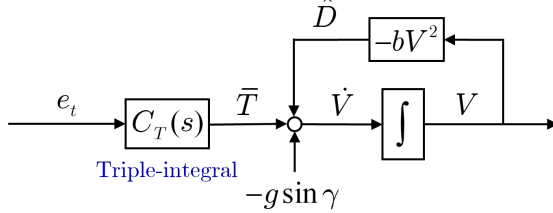


Fig. 8 Velocity dynamics of an aircraft

The second assumption ii) suggests that the derivative of the tangential position error is required to associate the velocity dynamics with a control signal; we firstly define the error variables as follows:

$$e := e_t, \quad e_1 := \int e, \quad e_2 := \iint e, \quad e_3 := \iiint e, \quad \dot{e} := \frac{d}{dt} e \quad (22)$$

Then we select the state variables as $\mathbf{e} := (e_3, e_2, e_1, e, \dot{e})$ and by using a chain of three integrators, the error dynamics can be represented in the state-space model (23) as

$$\frac{d}{dt} \begin{bmatrix} e_3 \\ e_2 \\ e_1 \\ e \\ \dot{e} \end{bmatrix} = \underbrace{\begin{bmatrix} 0 & 1 & 0 & 0 & 0 \\ 0 & 0 & 1 & 0 & 0 \\ 0 & 0 & 0 & 1 & 0 \\ 0 & 0 & 0 & 0 & 1 \\ 0 & 0 & 0 & 0 & 0 \end{bmatrix}}_{\mathbf{A}} \begin{bmatrix} e_3 \\ e_2 \\ e_1 \\ e \\ \dot{e} \end{bmatrix} + \underbrace{\begin{bmatrix} 0 \\ 0 \\ 0 \\ 0 \\ 1 \end{bmatrix}}_{\mathbf{B}} (\bar{T} - \dot{V}_o). \quad (23)$$

One should note that the system dynamics involve the derivative of the nominal velocity $\dot{V}_o = -g \sin \gamma_o$. We, however, can neglect the derivative of the nominal velocity as it is bounded and considered negligible compared to the thrust contribution, which is expected to grow parabolically to compensate for drag. Thus, the state-space model becomes a 5th-order linear system $\dot{\mathbf{e}} = \mathbf{A}\mathbf{e} + \mathbf{B}u$ where $u := \bar{T}$. Now our goal is to find a state feedback law (24) to drive the error vector to zero, i.e., $\mathbf{e} \rightarrow 0$. We choose

$$\bar{T} = -\mathbf{K}\mathbf{e} = -[k_Q \ k_R \ k_I \ k_P \ k_D] \mathbf{e}. \quad (24)$$

In our case, only the tangential position error e can be directly measured, and its first differentiation \dot{e} is estimated by taking the derivative with respect to time. A differentiation operation, however, is neither causal nor realizable. Hence,

we use a first-order approximated differentiator (APD) (25), cascading a pure differentiator and a lowpass filter (LPF), to take the derivative of the measured position errors.

$$G_{APD}(s) = \frac{s}{s/f_c + 1} = \underbrace{\frac{s}{\text{differentiator}}}_{\text{LPF}} \cdot \underbrace{\frac{1}{s/f_c + 1}}_{\text{LPF}} \quad (25)$$

we can also suppress high-frequency differentiation noise by properly selecting the cut-off frequency f_c . Note that the APD becomes the conventional differentiator as $f_c \rightarrow \infty$.

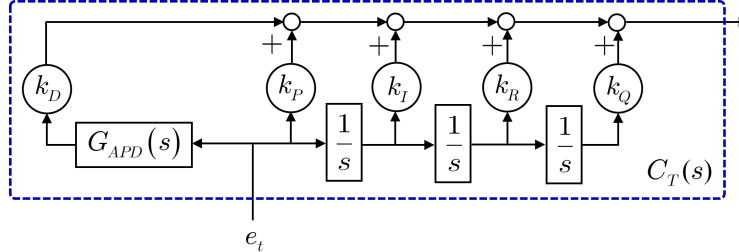


Fig. 9 Realization of the thrust controller (Adapted from [12])

The proposed thrust controller consists of three integrators used to reject the drag that is quadratically increasing with time and state feedback that stabilizes the system, as shown in Fig. 9. We assumed that the tangential position error is accessible and its derivative is estimated using APD, so the final step was to find the optimal state feedback control gain \mathbf{K} using LQR, such that $(\mathbf{A} - \mathbf{B}\mathbf{K})$ is Hurwitz. Finally, we needed to calculate the optimal gain \mathbf{K} that minimizes the quadratic cost function

$$J = \int_0^\infty (\mathbf{e}^T \mathbf{Q} \mathbf{e} + u^T \mathbf{R} u) dt \quad (26)$$

subject to the system dynamics $\dot{\mathbf{e}} = \mathbf{A}\mathbf{e} + \mathbf{B}u$, where $\mathbf{Q} = \mathbf{Q}^T \geq 0$ and $\mathbf{R} = \mathbf{R}^T > 0$ are weighting matrices to trade off the regulation performance and control effort. The optimal feedback gain \mathbf{K} can be derived by employing the maximum principle [42] as $\mathbf{K} = \mathbf{R}^{-1} \mathbf{B}^T \mathbf{P}$, where \mathbf{P} is the solution of the algebraic Riccati equation (27).

$$\mathbf{P}\mathbf{A} + \mathbf{A}^T \mathbf{P} - \mathbf{P}\mathbf{B}\mathbf{R}^{-1}\mathbf{B}^T \mathbf{P} + \mathbf{Q} = 0 \quad (27)$$

The tracking error and control input weighting matrices are chosen, based on a Boeing 777 model characteristic, as

$$\mathbf{Q} = \begin{bmatrix} 0.01 & 0 & 0 & 0 & 0 \\ 0 & 0.01 & 0 & 0 & 0 \\ 0 & 0 & 0.01 & 0 & 0 \\ 0 & 0 & 0 & 500 & 0 \\ 0 & 0 & 0 & 0 & 0.01 \end{bmatrix}, \quad R = 300.$$

The resulting optimal gain matrix \mathbf{K} is $[0.0058 \ 0.0776 \ 0.5185 \ 1.8762 \ 1.9371]$.

B. PID-based elevator control

Under the small angle-of-attack assumption, the flight path angle is approximately equal to the pitch angle; therefore, only pitch dynamics

$$\dot{\theta} = q, \quad \dot{q} = \frac{M(\delta_e)}{I_y} := \bar{M}$$

are considered when designing the moment (elevator) controller. Moreover, since the system is converted to minimum phase by moving the reference point from the CG to the cockpit, a traditional PID controller is applied to provide appropriate control. Thus, the pitch moment control law was determined to be

$$\bar{M} = k_{P_n} e_n + k_{I_n} \int e_n + k_{D_n} \frac{de_n}{dt} \quad (28)$$

where k_{P_n} , k_{I_n} and k_{D_n} are chosen, based on a Boeing 777 model characteristic, as 0.3, 0.5 and 3.2, respectively. The corresponding elevator deflection can be derived based on the relationship between the pitch moment coefficient and the elevator (12).

VI. Results and Analysis

We now present a numerical example using a Boeing 777 model [43] to illustrate and validate our proposed control framework. We selected the initial velocity and flight path angle as $(V_0, \gamma_0) = (600 \text{ (ft/s)}, 0.7854 \text{ (rad)})$ to derive the corresponding nominal zero-g trajectory. The state and control trajectories are presented in the following pages, see Fig. 11.

A. Numerical simulation

Figure 10 shows the entire zero-gravity maneuver containing the pull-up, parabola, and recovery phases, however, the controller is only employed at the parabola stage.

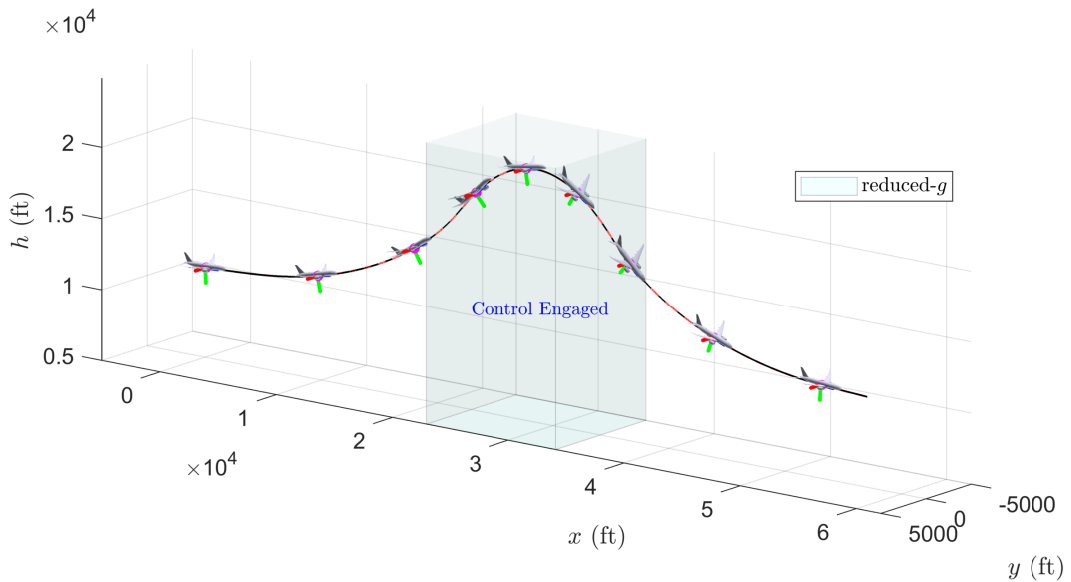
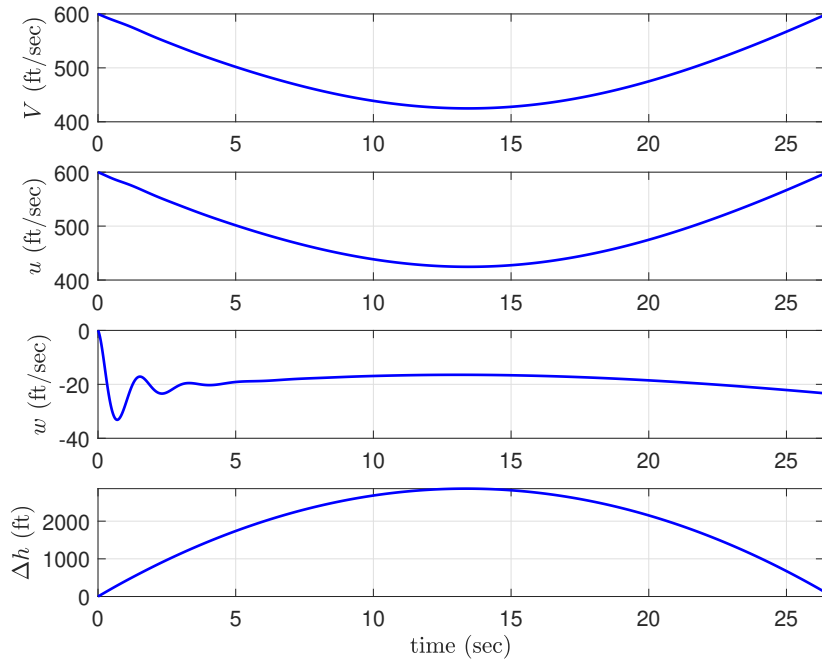


Fig. 10 Illustration of an entire zero-g flight maneuver: pull-up—parabola—recovery

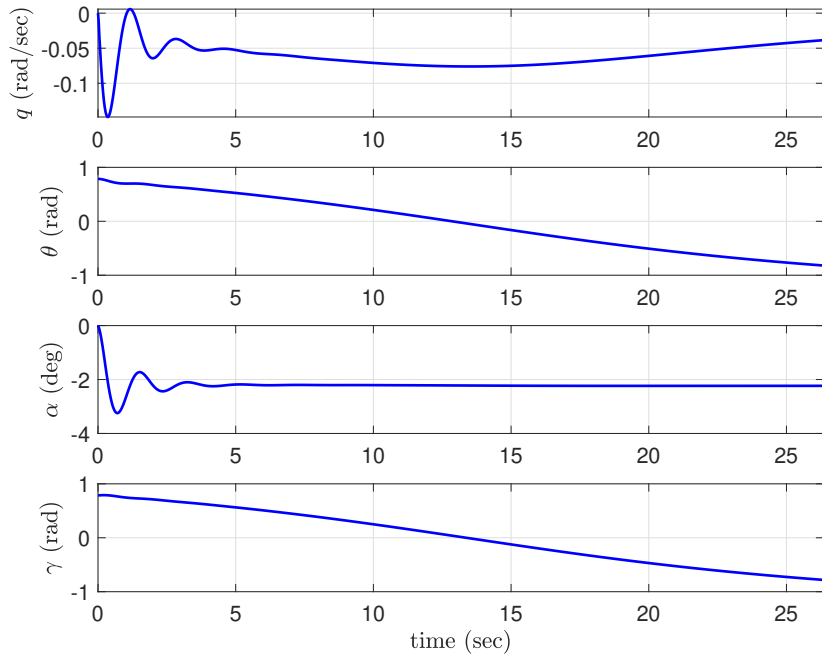
Figure 11a shows that the velocity time history is symmetric about the time at which the aircraft reaches the top of the parabola. It is seen that the short-period behavior is significant in the responses of the vertical velocity w , angle of attack α , and pitch rate q . Also, the angle of attack is indeed small (about -2 degrees) during the zero-g flight maneuver, as shown in Fig. 11b.

Figure 11c illustrates time histories of the position errors and the deviation from the nominal conditions. The nominal trajectory was calculated from the assigned initial condition, but it was not engaged in either the thrust or moment controller. Additionally, we can find that the tracking performance is compromised to decrease harsh changes in the control forces and local acceleration during the transient response.

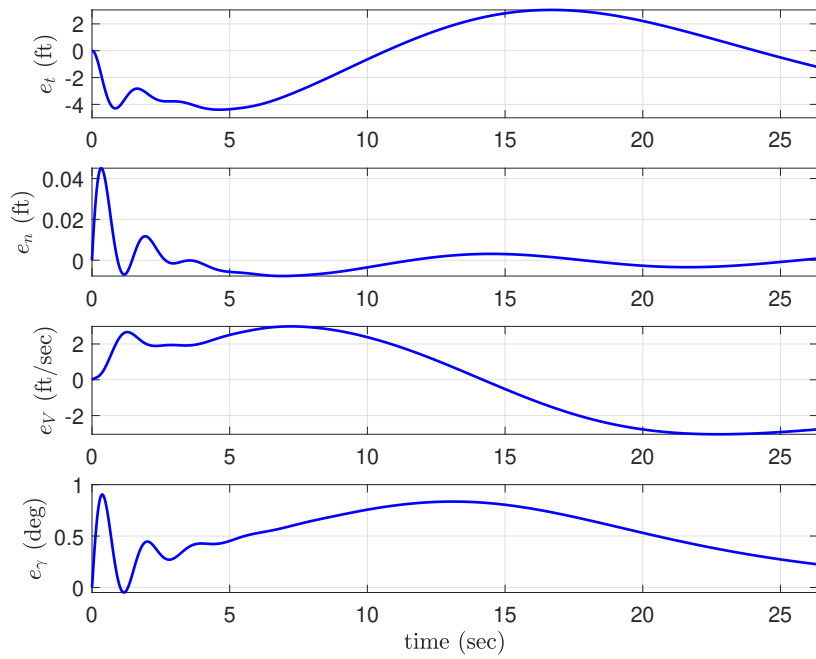
Finally, without taking any information about drag, thrust still grows quadratically with time (after entering the steady state) to minimize the longitudinal error and counteract the quadratically increasing drag, see Fig. 11d.



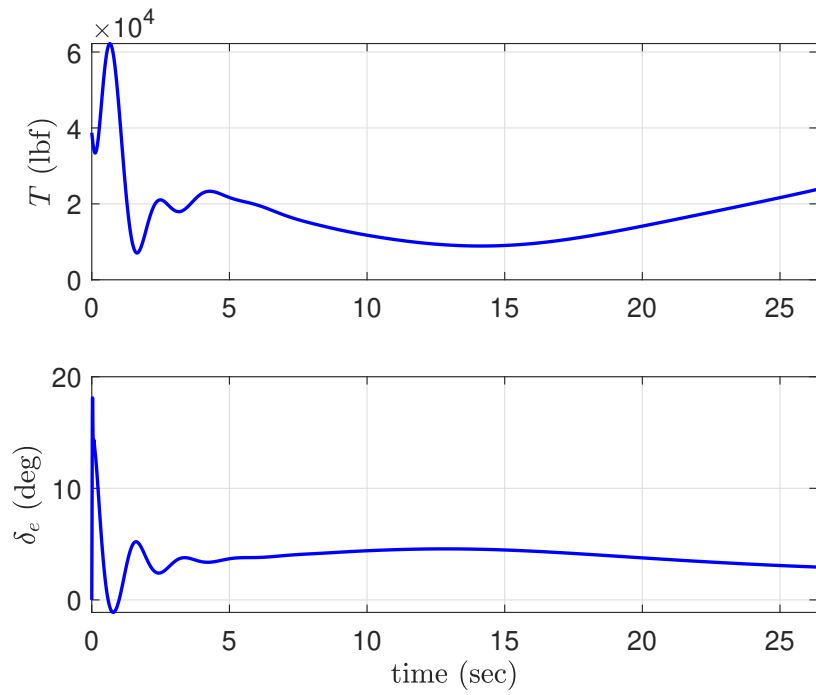
(a) Response of airspeed V , velocity components in the body frame u , w , and change of altitude Δh



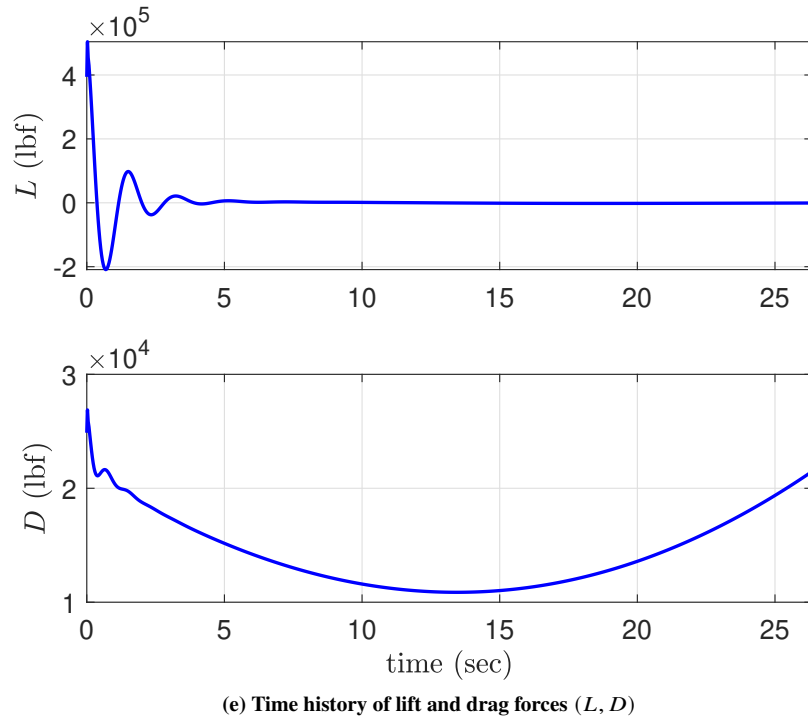
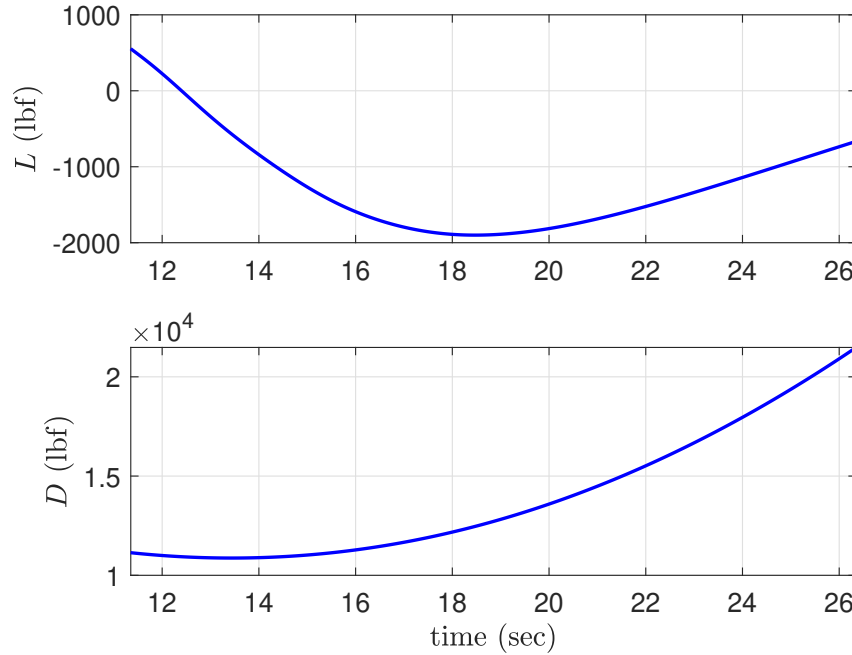
(b) Response of pitch rate q , pitch angle θ , angle of attack α , and flight path angle γ



(c) Position tracking errors (e_t, e_n) and the deviation from the nominal trajectory (e_V, e_γ)



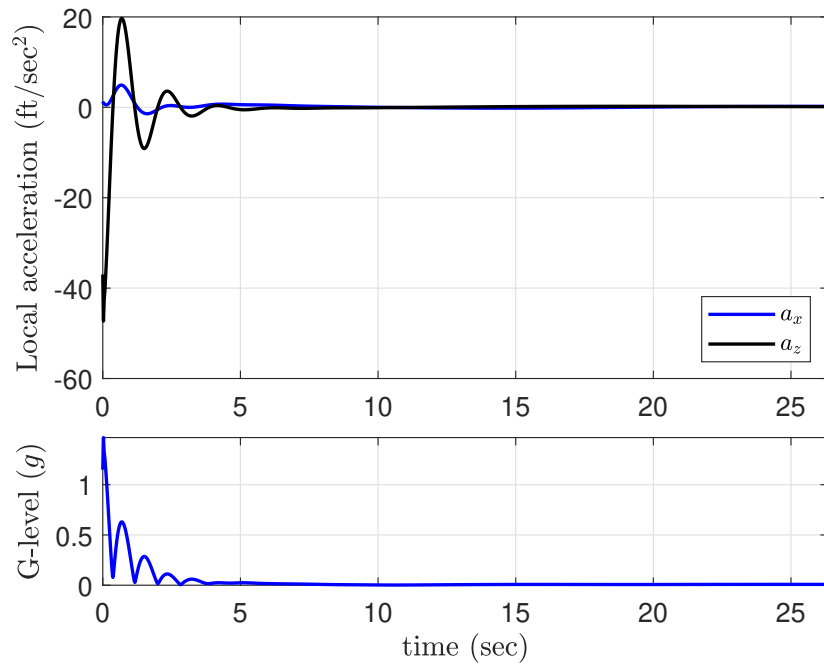
(d) Time history of control inputs $\mathbf{U} = (T, \delta_e)$

(e) Time history of lift and drag forces (L, D)

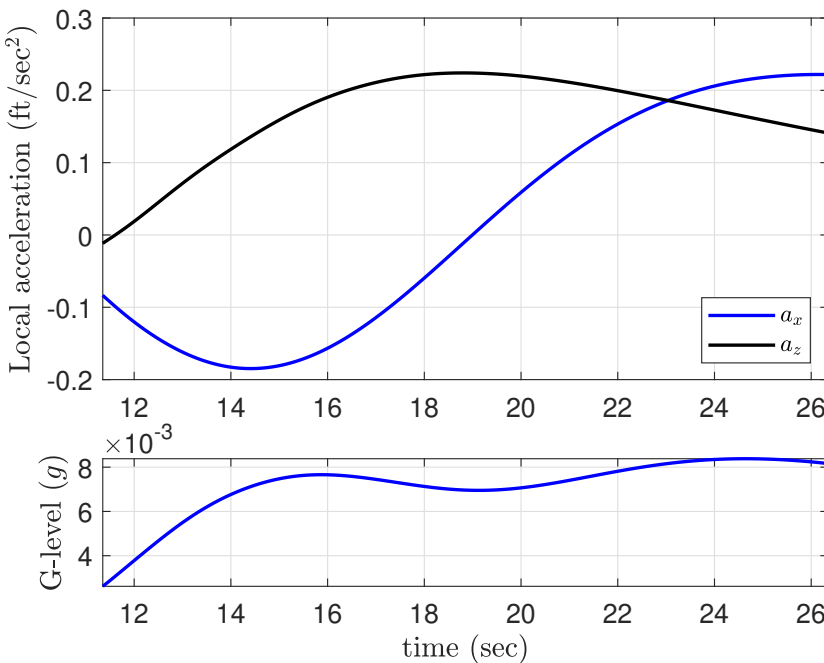
(f) Responses of lift and drag forces during the last 15 seconds of the zero-g maneuver

Fig. 11 Simulation result of the zero-gravity maneuver

According to the earlier discussion (16), lift force should approach zero during the zero-g maneuver. Figure 11e and 11f illustrate the evolution of aerodynamic forces; lift remains small to minimize the non-gravitational forces Z , while the drag increases quadratically in time, as expected.



(a) Time history of local acceleration at the CG



(b) Local acceleration at the CG during the last 15 seconds of the zero-g maneuver

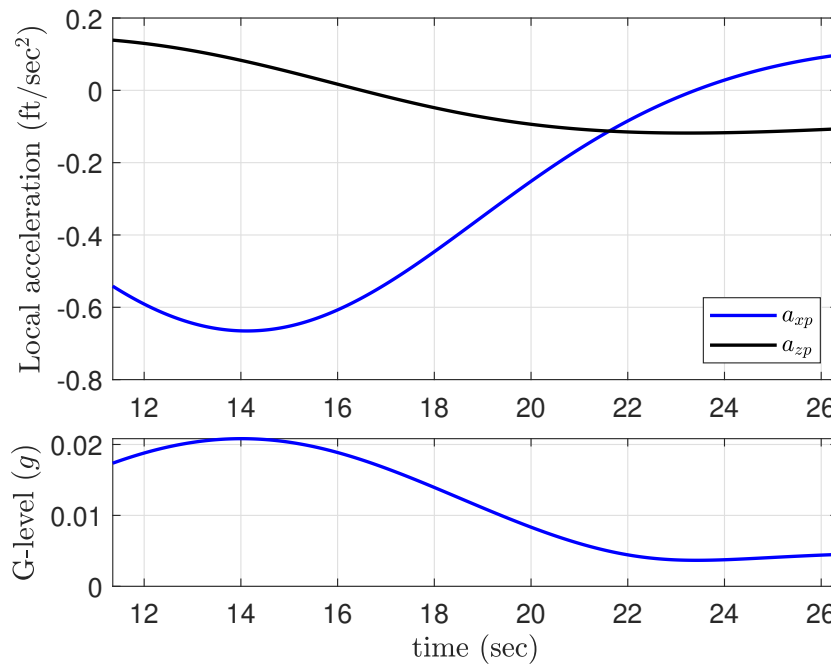
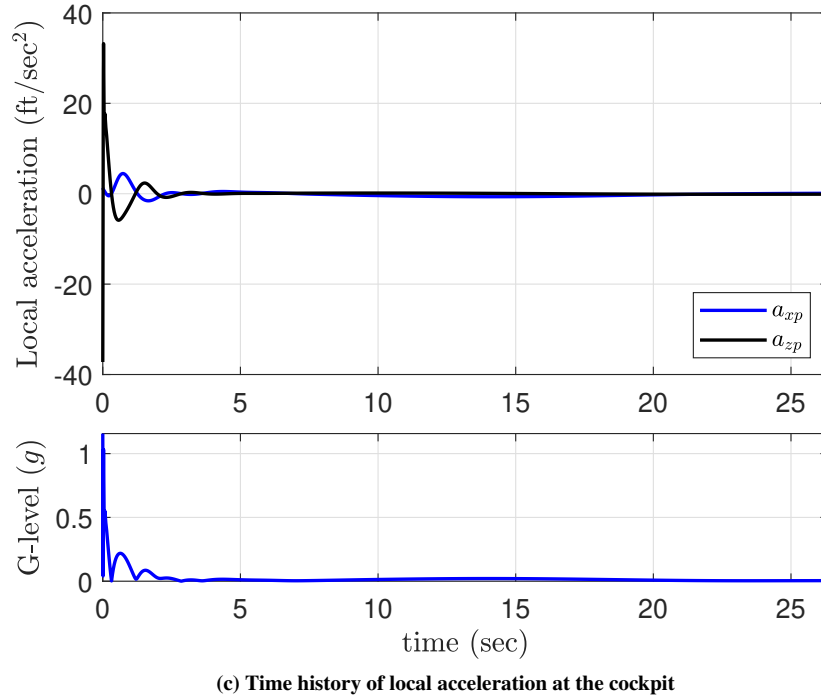


Fig. 12 Response curves of local acceleration and g -level

The most important result of the simulation — the acceleration that passengers at the CG and the cockpit will experience — is shown in Fig. 12. It can be seen that there is no large difference between the sensation of weight at the CG and the cockpit. Also, we can see the normal accelerations a_z and a_{zp} are affected significantly by the response of the elevator. These undesirable initial oscillations may be reduced by properly tuning the control gains or using

lead-lag compensation to smooth out the transient response. However, these figures still illustrate the feasibility of the proposed control architecture. The duration of microgravity at the CG is around 20 seconds with a residual g -level one-thousandth of Earth's gravity.

B. FlightGear visualization

In order to visualize the flight maneuver, we have to render the location (longitude, latitude, altitude) and orientation (roll, pitch, yaw) of the aircraft from Simulink to FlightGear [44]. Longitude and latitude can be obtained by using the navigation equations and geodetic position calculation as follows:

$$\dot{x} = V \cos \gamma = u \cos \theta + w \sin \theta$$

$$\dot{h} = V \sin \gamma = u \sin \theta - w \cos \theta$$

$$\dot{\phi} = \frac{V_N}{M + h}, \quad \dot{\lambda} = \frac{V_E}{(N + h) \cos \phi}$$

where V_N and V_E are the geographic system North and East components of velocity in the inertial Earth frame \mathcal{F}_E . In our case, V_N is equal to \dot{x} and V_E is equal to zero because only longitudinal motion is considered; M and N denote the meridian and prime vertical radii of curvatures. For a comprehensive discussion of the geodetic coordinate, we refer to [32] chapter 1.6. The screenshots of the zero-gravity maneuver are presented in Fig. 13.



Fig. 13 Visualization of a zero-gravity maneuver in FlightGear (video link: <https://youtu.be/94dRG9IPGZg>)

VII. Conclusion

This work investigates the general concept of simulating microgravity through reduced-gravity flights. In particular, we focus on the dynamic analysis for reduced-gravity flights and present a novel control framework for zero-gravity flight based on the proof-mass-tracking method. We start by discussing the operating principles of reduced-gravity flights and then study the passenger's sensation of weight by analyzing external forces acting on an aircraft.

Most importantly, using a free-falling proof mass as an inertial reference allows us to guide an aircraft towards a drag-free trajectory without the need for information on aerodynamic drag. In this scenario, only the position deviation from the nominal trajectory is required to calculate the corresponding thrust and the elevator deflection. Moreover, we place a proof mass in the cockpit rather than at the center of gravity to avoid non-minimum phase characteristics. Consequently, a PID-based compensation is applied for the moment (elevator) controller. However, more detailed investigation of non-minimum phase behavior needs to be conducted to improve elevator control response, i.e., reduce the oscillations that occur in transient response. At the same time, a thrust controller consisting of three integrators and state feedback was developed based on the characteristic of drag during zero-gravity maneuver. Lastly, we perform the numerical simulation to show the feasibility of the proposed control framework and to prove our conclusion that thrust will increase quadratically with time to counterbalance the unknown drag and the lift force maintain small simultaneously.

Acknowledgments

This research was funded by King Abdullah University of Science and Technology's baseline support.

References

- [1] Rogers, M. J., Vogt, G. L., and Wargo, M. J., "Microgravity: A Teacher's Guide with Activities in Science, Mathematics, and Technology," Tech. rep., 1997.
- [2] Karmali, F., and Shelhamer, M., "The dynamics of parabolic flight: flight characteristics and passenger percepts," *Acta Astronautica*, Vol. 63, No. 5-6, 2008, pp. 594–602.
- [3] Afman, J. P., and Feron, E., "A full scale atmospheric flight experimental research environment for Titan exploration devices," *Georgia Institute of Technology*, 2019.
- [4] Novespace, "NOVESPACE AND AVICO," , 2019. URL <https://www.airzerog.com/novespace-and-avico/>.
- [5] Zero-G, "Zero-G: Home," , 2022. URL <https://www.gozerog.com/>.
- [6] Pletser, V., "Are aircraft parabolic flights really parabolic?" *Acta Astronautica*, Vol. 89, 2013, pp. 226–228.
- [7] Martin, P., "Review of NASA's microgravity flight services," Tech. rep., Technical Report, NASA, IG-10-015, 2010.
- [8] LANGE, B., "The Drag-Free Satellite," *AIAA Journal*, Vol. 2, No. 9, 1964, pp. 1590–1606. <https://doi.org/10.2514/3.55086>, URL <https://doi.org/10.2514/3.55086>.
- [9] DeBra, D. B., "Drag-free spacecraft as platforms for space missions and fundamental physics," *Classical and Quantum Gravity*, Vol. 14, No. 6, 1997, pp. 1549–1555. <https://doi.org/10.1088/0264-9381/14/6/026>, URL <https://doi.org/10.1088/0264-9381/14/6/026>.
- [10] Afman, J.-P., Franklin, J., Mote, M. L., Gurriet, T., and Feron, E., "On the Design and Optimization of an Autonomous Microgravity Enabling Aerial Robot," *arXiv preprint arXiv:1611.07650*, 2016.
- [11] Afman, J.-P., Feron, E., and Hauser, J., "Maneuver Regulation for Accelerating Bodies in Atmospheric Environments," *arXiv preprint arXiv:1708.01838*, 2017.
- [12] Afman, J.-P., Feron, E., and Hauser, J., "Triple-integral control for reduced-g atmospheric flight," *2018 Annual American Control Conference (ACC)*, IEEE, 2018, pp. 392–397.
- [13] Kraeger, A., and van Paassen, M., "Micro-and Partial Gravity Atmospheric Flight," *AIAA Atmospheric Flight Mechanics Conference*, American Institute of Aeronautics and Astronautics Inc. (AIAA), United States, 2002, pp. 1–11. Paper 2002-4499.
- [14] Hathaway, J. D., and Jacob, J. D., "Development of a Microgravity Generating Flight Mode for UAS," *AIAA Modeling and Simulation Technologies Conference*, 2016, p. 3219.

- [15] Herranz, R., Anken, R., Boonstra, J., Braun, M., Christianen, P. C., de Geest, M., Hauslage, J., Hilbig, R., Hill, R. J., Lebert, M., et al., “Ground-based facilities for simulation of microgravity: organism-specific recommendations for their use, and recommended terminology,” *Astrobiology*, Vol. 13, No. 1, 2013, pp. 1–17.
- [16] Sanavandi, H., and Guo, W., “A magnetic levitation based low-gravity simulator with an unprecedented large functional volume,” *npj Microgravity*, Vol. 7, No. 1, 2021, pp. 1–7.
- [17] Mora-Camino, F., and Achaibou, A. K., “Zero-gravity atmospheric flight by robust nonlinear inverse dynamics,” *Journal of Guidance, Control, and Dynamics*, Vol. 16, No. 3, 1993, pp. 604–607. <https://doi.org/10.2514/3.21056>, URL <https://doi.org/10.2514/3.21056>.
- [18] Amato, F., Ambrosino, G., Garofalo, F., and Verde, L., “A flight control system for microgravity experiments,” *[Proceedings 1992] The First IEEE Conference on Control Applications*, 1992, pp. 351–353, vol.1. <https://doi.org/10.1109/CCA.1992.269850>.
- [19] Amato, F., Ambrosino, G., Mattei, M., and Verde, L., “Design and robustness analysis of gain-scheduled control system for parabolic flight,” *Journal of Guidance, Control, and Dynamics*, Vol. 19, No. 2, 1996, pp. 430–437. <https://doi.org/10.2514/3.21636>, URL <https://doi.org/10.2514/3.21636>.
- [20] D’Antonio, L., and Monaco, S., “A nonlinear controller for parabolic flight,” *Proceedings of 32nd IEEE Conference on Decision and Control*, 1993, pp. 1513–1518 vol.2. <https://doi.org/10.1109/CDC.1993.325441>.
- [21] Hosman, R., and Kunen, R., “Flight director guidance throughout the parabolic maneuver,” *IEEE SMC’99 Conference Proceedings. 1999 IEEE International Conference on Systems, Man, and Cybernetics (Cat. No.99CH37028)*, Vol. 5, 1999, pp. 1076–1081 vol.5. <https://doi.org/10.1109/ICSMC.1999.815706>.
- [22] Brigos, M., Perez-Poch, A., Alpiste, F., Torner, J., and González Alonso, D. V., “Parabolic flights with single-engine aerobatic aircraft: flight profile and a computer simulator for its optimization,” *Microgravity science and technology*, Vol. 26, No. 4, 2014, pp. 229–239.
- [23] Kraeger, A. M., “Free-Wing Unmanned Aerial Vehicle as a Microgravity Facility,” *Journal of Guidance, Control, and Dynamics*, Vol. 29, No. 3, 2006, pp. 579–587. <https://doi.org/10.2514/1.2274>, URL <https://doi.org/10.2514/1.2274>.
- [24] Higashino, S.-i., and Kozai, S., “Automatic microgravity flight system and flight testing using a small unmanned aerial vehicle,” *Journal of The Japan Society of Microgravity Application*, Vol. 27, No. 1, 2010, p. 3.
- [25] Hofmeister, P. G., and Blum, J., “Parabolic flights @ home,” *Microgravity Science and Technology*, Vol. 23, No. 2, 2011, pp. 191–197.
- [26] Afman, J.-P., Feron, E., and Hauser, J., “Nonlinear maneuver regulation for reduced-g atmospheric flight,” *2018 IEEE Conference on Decision and Control (CDC)*, IEEE, 2018, pp. 731–736.
- [27] Kedarisetty, S., “Autonomous Reduced-Gravity Enabling Quadrotor Test-bed: Design, Modelling and Flight test Analysis,” *Aerospace Science and Technology*, Vol. 86, 2019. <https://doi.org/10.1016/j.ast.2019.01.014>.
- [28] Kedarisetty, S., “Model Based Robust Control and Automation Design for a Micro-Gravity Enabling Multi-Rotor Test Bed,” *AIAA Scitech 2019 Forum*, 2019, p. 1171.
- [29] Kedarisetty, S., and Manathara, J. G., “Acceleration control of a multi-rotor UAV towards achieving microgravity,” *Aerospace Systems*, Vol. 2, No. 2, 2019, pp. 175–188.
- [30] AirZeroG, “How does zero-gravity parabolic flights work?”, 2019. URL <https://www.airzerog.com/zero-g-flights-how-it-works/>.
- [31] European Space Agency, “Parabolic manoeuvres,” https://www.esa.int/Education/Fly_Your_Thesis/Parabolic_manoeuvres, May 2020.
- [32] Stevens, B. L., Lewis, F. L., and Johnson, E. N., *Aircraft control and simulation: dynamics, controls design, and autonomous systems*, John Wiley & Sons, 2015.
- [33] Nelson, R. C., et al., *Flight stability and automatic control*, Vol. 2, WCB/McGraw Hill New York, 1998.
- [34] Etkin, B., and Reid, L. D., *Dynamics of flight*, Vol. 2, Wiley New York, 1959.
- [35] Gavilan, F., Vazquez, R., and Acosta, J. Á., “Adaptive control for aircraft longitudinal dynamics with thrust saturation,” *Journal of guidance, control, and dynamics*, Vol. 38, No. 4, 2015, pp. 651–661.

- [36] Maine, R. E., and Iliff, K. W., "Application of parameter estimation to aircraft stability and control: The output-error approach," Tech. rep., 1986.
- [37] Tomlin, C., Lygeros, J., Benvenuti, L., and Sastry, S., "Output tracking for a non-minimum phase dynamic CTOL aircraft model," *Proceedings of 1995 34th IEEE Conference on Decision and Control*, Vol. 2, 1995, pp. 1867–1872 vol.2. <https://doi.org/10.1109/CDC.1995.480615>.
- [38] Hauser, J., Sastry, S., and Meyer, G., "Nonlinear control design for slightly non-minimum phase systems: Application to V/STOL aircraft," *Automatica*, Vol. 28, No. 4, 1992, pp. 665–679.
- [39] Elkhatem, A., Engin, S. N., Pasha, A. A., Rahman, M. M., and Pillai, S. N., "Robust Control for Non-Minimum Phase Systems with Actuator Faults: Application to Aircraft Longitudinal Flight Control," *Applied Sciences*, Vol. 11, No. 24, 2021, p. 11705.
- [40] Kim, S., and Horspool, K. R., "Nonlinear controller design for non-minimum phase flight system enhanced by adaptive elevator algorithm," *AIAA Scitech 2020 Forum*, 2020, p. 0603.
- [41] Ma'arif, A., Cahyadi, A. I., Herdjunanto, S., and Wahyunggoro, O., "Tracking Control of High Order Input Reference Using Integrals State Feedback and Coefficient Diagram Method Tuning," *IEEE Access*, Vol. 8, 2020, pp. 182731–182741. <https://doi.org/10.1109/ACCESS.2020.3029115>.
- [42] Murray, R. M., et al., "Optimization-based control," *California Institute of Technology*, CA, 2009, pp. 111–128.
- [43] López Pereira, R., "Validation of software for the calculation of aerodynamic coefficients: with a focus on the software package Tornado," *Department of Management and Engineering Linköpings universitet*, 2010.
- [44] Lum, C., "Visualizing the State of a Simulink Aircraft Model Using FlightGear," , 2020. URL <https://www.youtube.com/watch?v=f8tdTiu5lo&list=PLxdnSsBqCrrEx3A6W94sQGClk6Q4YCg-h&index=24>.